Corrosion Science 136 (2018) 221–230

Contents lists available at ScienceDirect

Corrosion Science

journal homepage: www.elsevier.com/locate/corsci

Corrosion behavior of non-equilibrium Zr-Sn-Nb-Fe-Cu-O alloys in high-temperature 0.01 M LiOH aqueous solution and degradation of the surface oxide films

Liang-Yu Chen[a,b,c,*], Peng Shen[b], Lina Zhang[a], Sheng Lu[b], Linjiang Chai[d,**], Zhinan Yang[e], Lai-Chang Zhang[c,**]

[a] School of Science, Jiangsu University of Science and Technology, Zhenjiang, Jiangsu 212003, China
[b] School of Material Science and Engineering, Jiangsu University of Science and Technology, Zhenjiang Jiangsu 212003, China
[c] School of Engineering, Edith Cowan University, 270 Joondalup Drive, Joondalup, Perth, WA 6027, Australia
[d] College of Materials Science and Engineering, Chongqing University of Technology, Chongqing 400054, China
[e] National Engineering Research Center for Equipment and Technology of Cold Strip Rolling, Yanshan University, Qinhuangdao 066004, China

ARTICLE INFO

Keywords:
A. Zirconium
B. SEM
B. TEM
B. Nanoscratch
C. High temperature corrosion
C. Oxidation

ABSTRACT

This work uses qualitative analyses to investigate the corrosion behavior of two non-equilibrium Zr-Sn-Nb-Fe-Cu-O alloys in 0.01 M LiOH aqueous solution at 360 °C/18.6 MPa. Precipitates of second-phase particles (SPPs) and local recrystallization in the matrix are observed near the oxide/metal interface during extended periods of corrosion. Oxides formed on both alloys exhibit different hardness and gradually degrade. The oxides embedded with more SPPs show a lower hardness and therefore break down earlier. The variations of non-equilibrium microstructures of the substrates influence the properties of the oxides, thereby determining the corrosion performance of the alloys.

1. Introduction

At high temperature and high pressure in water or LiOH aqueous solutions, oxides form on the zirconium alloys and grow continuously in association with a decreasing corrosion rate [1–8]. Under these conditions, the weight gain of zirconium alloys primarily follows a cubic or parabolic law [7,8]. After a certain time, a rapid increase in the weight gained by the alloys could be observed: such a phenomenon is known as the transition in corrosion kinetics [9,10]. However, weight gain is not the sole criterion for evaluating the corrosion resistance of zirconium alloys that are corroded in water or LiOH aqueous solutions under conditions of high temperature and high pressure. For example, although several zirconium alloys (such as Zr-Nb alloys) were reported to demonstrate similar weight gain before the transition in corrosion kinetics under the same testing conditions, the best corrosion resistance within the test time was observed in the alloy that went through the transition last of all [9–13].

Many researchers have studied the corrosion behavior of zirconium alloys in water or LiOH aqueous solutions under conditions of high temperature and high pressure [9,10,14–20]. For example, Wei et al. [10] systematically investigated the effect of Sn on corrosion mechanisms in Zr-Sn-Nb alloys corroded at 360 °C/18 MPa in simulated primary water and proposed that Sn can stabilize the tetragonal ZrO_2 phase, thus reducing the pre-transition time; Garner et al. [9] and Wenman et al. [14] interpreted this result in terms of the microtexture of the oxides and density function theory (DFT). Wang et al. [15] found that those cations (Y^{3+}, Fe^{3+}) which have larger diffusion coefficients in ZrO_2 than Zr^{4+} would trigger the Kirkendall effect, resulting in nanoscale porosities in the oxides formed on zirconium alloys in 0.01 M LiOH aqueous solution at 360 °C/18.6 MPa; the oxides with nanoscale porosities were more prone to delaminate than the counterparts without porosity. Hu et al. [16] corroded $(Zr, Nb)_2Fe$ alloy in simulated reactor conditions and pointed out that Fe^{3+} can also stabilize the tetragonal ZrO_2 phase. Bell et al. [17] studied the valences of Nb ions under different oxygen partial pressures by DFT and showed the effects of Nb ions on the corrosion behavior and the hydrogen pick-up behavior of the alloy in various valences. Huang et al. [18,19] investigated the corrosion behavior of Zr-0.8Sn-1.0Nb-0.3Fe-0.1Cr-xS (in wt.%; the same hereafter unless otherwise indicated) and 90Nb-10Zr alloys by analyzing the precipitates of second-phase particles (SPPs), pointing out that various SPPs have different oxidation rates. Škarohlíd et al. [20] coated Zr-0.9Sn-0.9Nb-0.1Fe alloys with nanocrystalline diamond

* Corresponding author at: School of Science, Jiangsu University of Science and Technology, Zhenjiang, Jiangsu 212003, China.
** Corresponding authors.
E-mail addresses: lychen@just.edu.cn (L.-Y. Chen), chailinjiang@cqut.edu.cn (L. Chai), l.zhang@ecu.edu.au (L.-C. Zhang).

https://doi.org/10.1016/j.corsci.2018.03.012
Received 20 September 2017; Received in revised form 6 March 2018; Accepted 8 March 2018
Available online 13 March 2018
0010-938X/

layers and found that the uptake of oxygen and hydrogen was effectively mitigated in water at 360 °C/16 MPa.

Manipulation of the processing procedure is also a useful method to optimize the performance of zirconium alloys by tailoring the microstructures [11,13,21–24]. Ly et al. [21] found that the pre-transition time of recrystallized Zircaloy-4 (Zr-1.25Sn-0.2Fe-0.1Cr-0.13O) alloy in primary water at 360 °C/18 MPa reduced as the final annealing temperature increased, which resulted in increase in grain size of the substrate. On account of this result, Likhanskii et al. [22,23] established a model on the basis of elastic energy minimization to evaluate the transition in corrosion kinetics of zirconium alloys. They provided evidence that this transition is related to the undulations of the oxide/metal interface. By analyzing data relating to correlations between the length of the lateral cracks in the oxides and the amplitude of the undulations, Chen et al. [11,13] pointed out that Zr-0.4Sn-0.35Nb-0.3Fe-0.08O and Zr-0.4Sn-0.35Nb-0.3Fe-0.05Cu-0.08O alloys, which underwent a final annealing at recovery temperature after cold rolling, would experience a postponed transition in corrosion kinetics in both water and 0.01 M LiOH aqueous solution at 360 °C/18.6 MPa. For HANA-6 alloy (Zr-1.1Nb-0.05Cu), experimental results also proved that the alloy with low-temperature final annealing (about 470 °C) had a longer pre-transition time than that with high-temperature final annealing (about 570 °C) when HANA-6 was corroded in pure water at 360 °C [24]. These researches enhanced the corrosion resistance of zirconium alloys; however, there was no overall understanding of the degradation of the oxides formed on non-equilibrium zirconium alloys processed by low-temperature final annealing.

In general, the emergence of pores and cracks is the precondition for the degradation of oxides, which finally leads to the transition in corrosion kinetics of zirconium alloys under conditions of high temperature and high pressure [25–29]. Therefore, further understanding of the relationship between the properties of the oxides grown from metal substrates and the corrosion behavior of zirconium alloys is the main objective of the work described in this paper. In this work, two Zr-Sn-Nb-Fe-Cu-O alloys composed of non-equilibrium microstructures with different Nb contents were selected. The microstructures of the alloys were studied. The properties of the oxides formed on the alloys in 0.01 M LiOH aqueous solution at 360 °C/18.6 MPa were investigated by nanoscratch tests. Pertinent factors in the transition in corrosion kinetics of zirconium alloys were evaluated.

2. Experimental

2.1. Material preparation

Two zirconium alloys with nominal chemical compositions of Zr-0.4Sn-0.35Nb-0.3Fe-0.05Cu-0.08O (denoted as Zr-0.35Nb) and Zr-0.4Sn-1Nb-0.3Fe-0.05Cu-0.08O (denoted as Zr-1Nb) were prepared by vacuum arc re-melting three times to obtain chemical homogeneity. Both alloys were corroded in an isothermal static autoclave in 0.01 M LiOH aqueous solution at 360 °C under a saturation pressure of 18.6 MPa after processing. The chemical compositions of Zr-0.35Nb and Zr-1Nb alloys are listed in Table 1. The disk-shape ingots were forged to 10 mm thick at 1000 °C and β-quenched at 1050 °C. The as-quenched samples were then hot-rolled, intermediate annealed at 570 °C for 1 h and cold-rolled to 1.8 mm. At this point, the second β-quenching processing was used instead of intermediate annealing. Afterward, the samples were cold-rolled twice to a final thickness of 0.6 mm accompanied by intermediate annealing of 470 °C for 1 h. Finally, the samples were annealed at temperature of 470 °C for 5 h. Each stage of the procedure is summarized in Fig. 1.

Table 1
Chemical compositions (in wt.%) of Zr-0.35Nb and Zr-1Nb alloys.

Alloy	Elements					
	Zr	Sn	Fe	Nb	Cu	O
Zr-0.35Nb	Balance	0.55	0.32	0.35	0.05	0.079
Zr-1Nb	Balance	0.54	0.33	1.01	0.05	0.082

2.2. Autoclave corrosion

The samples used for the corrosion test were 15 mm × 20 mm in size and chemically polished using a pickling solution containing H_2O: HNO_3: H_2SO_4: HF of 3:3:3:1 (in vol.%, unless otherwise indicated) at 30–50 °C, then cleaned by pure water. The concentrations of HNO_3, H_2SO_4 and HF used were 68%, 98% and 40%, respectively. The corrosion resistance of the samples was evaluated by measuring their weight gain per unit surface area as a function of the exposure time, such as 3, 14, 42, 70, 100, 130, 160 and 200 days. The corroded samples were named after their exposure time (e.g. Zr-0.35Nb-100 stands for the Zr-0.35Nb sample after 100-day exposure, and so on). The corrosion test was conducted with an isothermal static autoclave in 0.01 M LiOH aqueous solution at 360 °C under a saturation pressure of 18.6 MPa according to ASTM-G2/02 [30].

2.3. Microstructure characterization

Microstructures of the alloys were characterized by using a FEI Sirion 200 field emission gun scanning electron microscope (SEM) and a JEOL-2100F transmission electron microscope (TEM). The samples for SEM observations were mechanically ground with SiC paper up to 2000 grits and polished to a mirror surface by a diamond paste with a particle size of 1.5 μm in a polishing machine, then etched in a solution containing H_2O: HNO_3: HF of 9: 9: 2 for about 15 s. The alloy specimens for TEM observations were prepared using a twin-jet polishing machine with a solution containing C_2H_5OH: $HClO_4$ of 9:1 at a voltage of 20 V and a temperature of − 30 °C. The concentrations of C_2H_5OH and $HClO_4$ used were 99.7% and 72%, respectively. The cross-sectional specimens of the oxides for TEM observations were prepared according to the following procedures. Two transverse cross-sectional segments of about 1 mm width were cut from the 100-day corroded samples, then glued together and inserted into a titanium tube of 3 mm diameter, fixed in place with epoxy. Slices (about 0.5 mm thick) were cut from the as-prepared titanium tube to provide some disks. Both sides of the disk sample were manually ground using 4000-grit SiC paper to a thickness of ~40 μm. The final thinning was performed using a Gatan Model 691 PIPS (Precision Ion Polishing System) instrument. The crystallographic characteristics of second-phase particles were determined by high resolution TEM (HRTEM) and analyzed using the software Image-Pro Plus 5.0.

2.4. Tensile tests

Tensile tests were performed using a Zwick Z100/SN3A universal testing machine in air at room temperature and 380 °C, respectively. Dog-bone flat tensile samples with a nominal gauge length of 15 mm and a cross section of 12 mm × 0.6 mm were cut parallel to the rolling direction by electric discharge machining from the alloy samples. The samples were subsequently mechanically ground with SiC paper up to 2000 grits. A displacement rate of 1 mm/min (nominal strain rate of $0.001\ s^{-1}$) was used for all the tensile tests.

2.5. Nanoscratch tests

Nanoscratch tests were carried out using the scratch option available in the CSM-NHT2 machine platform equipped with a Rockwell indenter with a 100 μm tip radius. In the tests, each specimen was moved against the static and loaded indenter at a speed of 10 mm/min for a total length of 5 mm. The tests were conducted in a linear loading

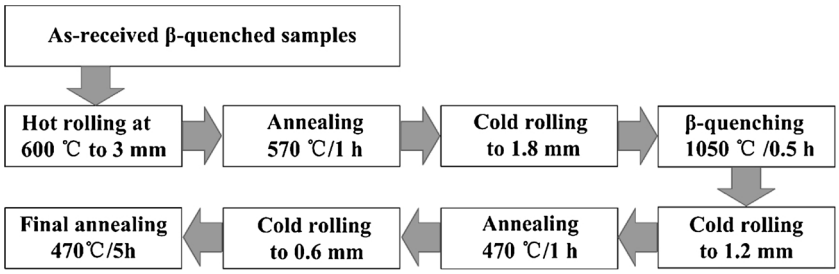

Fig. 1. Process flow of experimental alloys. Both alloy samples underwent the second β-quenching processing instead of intermediate annealing after the samples were cold-rolled to 1.8 mm. Afterward, the samples were cold-rolled twice to the final thickness of 0.6 mm accompanied by intermediate annealing of 470 °C for 1 h and final annealing of 470 °C for 5 h.

mode. The load increased progressively from 0.03 N to a maximum load of 10 N at a loading rate of 0.333 N/s. The 3-day, 42-day, 100-day and 130-day corroded samples were conducted on the nanoscratch tests. The images of the scratch tracks were obtained using an optical microscope attached to the CSM-NHT2 machine. Penetration depth and acoustic emission as a function of loaded normal force (displacement of specimen) were used to characterize the properties of the oxides. For the slope obtained on the penetration depth curve, the uncertainty was within 10%. Although nanoscratch tests were always used to examine the adhesion strength between the films and their substrates, other properties (such as cohesion of films and flaws) could also be detected qualitatively [31,32]. Therefore, the work reported in this paper adopted this method to test the properties of the oxides formed on Zr-0.35Nb and Zr-1Nb in 0.01 M LiOH aqueous solution at 360 °C/18.6 MPa.

3. Results

3.1. Microstructures and weight gain of experimental alloys

Fig. 2 shows the representative microstructural characteristics of the studied alloys. Both Zr-0.35Nb and Zr-1Nb reveal non-equilibrium partially recrystallized microstructures. The lath structure, which results from β-quenching, is still reserved in Zr-0.35Nb and no SPPs are observed (Fig. 2a). A similar phenomenon was reported in Zr-0.35Nb in our previous study [11]. For Zr-1Nb, the lath structure associated with about 0.2 vol.% SPPs is illustrated in Fig. 2b, as indicated by the solid white arrows. In previous reports [11,33–35], the alloys containing comparable contents of alloying elements would have about 2–10 vol.% SPPs after annealing at the recrystallization temperature. In this work, almost no precipitates can be observed in Zr-0.35Nb. The amount of SPPs detected in Zr-1Nb is only 0.2%, which is much lower than those mentioned in the papers [11,33–35]. As such, one can infer that Zr-0.35Nb and Zr-1Nb after final annealing are still in an oversaturated solid solution state.

TEM examinations were also carried out to further detail the microstructures of the studied alloys. As shown from Fig. 2c and d, the microstructures of both alloys are extremely similar. The lath structures accompanied by abundant dislocations are found in both alloys. This is ascribed to the second β-quenching and the subsequent cold rolling. Because of the low-temperature final annealing, the progress of recrystallization becomes sluggish in both alloys, leading to the conservation of the lath structures. It is important to note that SPPs could not be observed in Fig. 2c. In Fig. 2d, a small number of tiny SPPs can be found, as indicated by white arrows. The TEM results are consistent with those in the SEM observations. Therefore, one can conclude that

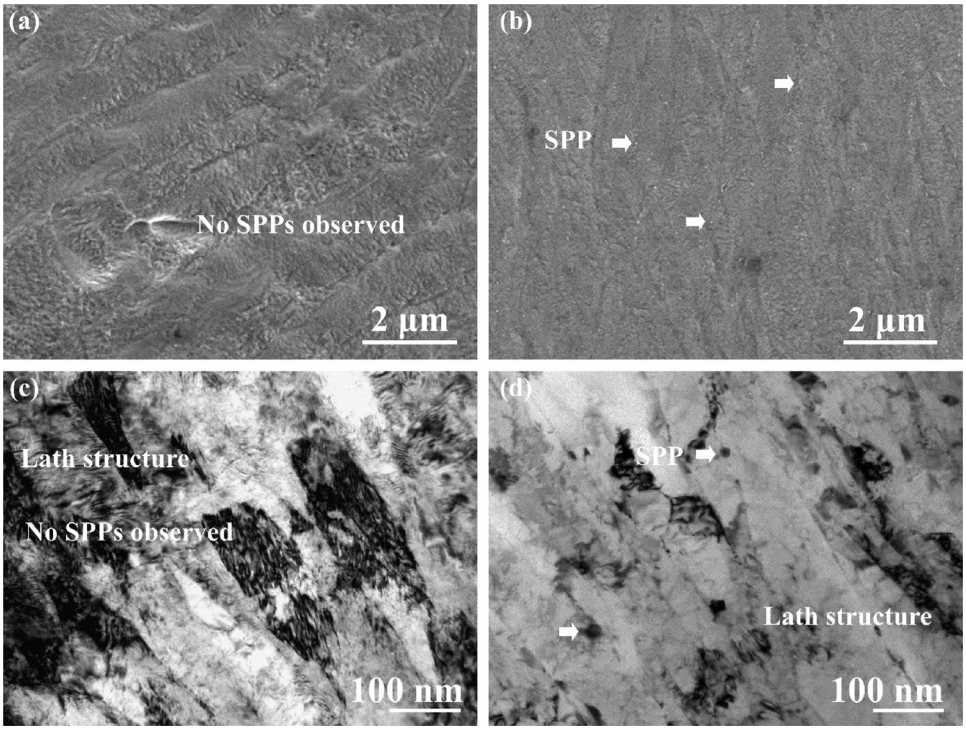

Fig. 2. SEM micrographs of (a) Zr-0.35Nb, (b) Zr-1Nb alloy samples and TEM micrographs of the typical microstructures for (c) Zr-0.35Nb and (d) Zr-1Nb alloy samples. The lath structures are observed both in Zr-0.35Nb and Zr-1Nb. However, no second-phase particles (SPPs) are observed in Zr-0.35Nb and only 0.2 vol.% SPPs are detected in Zr-1Nb.

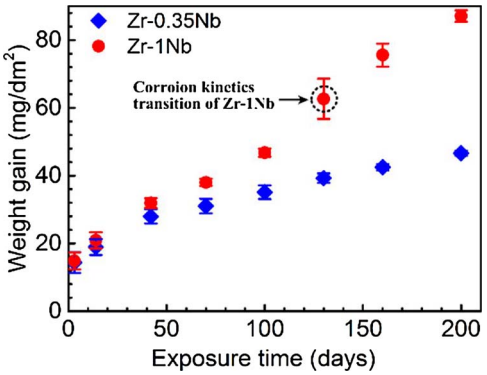

Fig. 3. Autoclave corrosion weight gain profiles for Zr-0.35Nb and Zr-1Nb in 0.01 M LiOH aqueous solution at 360 °C/18.6 MPa during 200-day exposure. Zr-1Nb shows a post-transition phenomenon after 100-day exposure, whereas Zr-0.35Nb exhibits no apparent sign of the transition in corrosion kinetics up to 200-day exposure. Scatter bands represent the standard deviations of five independent samples.

most alloying elements are still in solid solution in both alloys prior to corrosion test.

Fig. 3 reveals the corrosion weight gain of the alloys as a function of exposure time after the autoclave test in 0.01 M LiOH aqueous solution at 360 °C/18.6 MPa. The weight gain of both alloys follows a parabolic law before the transition in corrosion kinetics. The corrosion rate of Zr-1Nb is a slightly higher than that of Zr-0.35Nb, since the weight gain of both alloys is almost the same at 3-day exposure. The gap of weight gain in both alloys becomes larger as the exposure time increases. After 100-day exposure, a relatively rapid increase in weight gain is observed in Zr-1Nb. With up to 200-day exposure, Zr-0.35Nb shows no apparent sign of the transition in corrosion kinetics. Under the same testing conditions, higher corrosion resistance is often related to a longer pre-transition period, if there is no significant difference in weight gain of the alloys before the first transition [13,15,21,35–38]. Hence it means that Zr-0.35Nb possesses better corrosion resistance than Zr-1Nb in 0.01 M LiOH aqueous solution at 360 °C/18.6 MPa under 200-day exposure, although both alloys have been subjected to an identical processing procedure and have similar microstructure after final annealing.

3.2. Mechanical properties

Table 2 shows the tensile results for both alloys in air at room temperature and at 380 °C. At room temperature, the ultimate tensile strengths of Zr-0.35Nb and Zr-1Nb are 590 MPa and 698 MPa, respectively. At 380 °C, the tensile strengths of both alloys decrease (380 MPa for Zr-0.35Nb and 446 MPa for Zr-1Nb). The Zr-0.35Nb exhibits much higher tensile strength than its recrystallized counterpart [13]. Such a discrepancy is ascribed to the formation of a partially recrystallized structure coupled with a large number of dislocations in the alloy during low-temperature final annealing after cold work. At both test temperatures, Zr-1Nb exhibits slightly higher strengths than Zr-0.35Nb, which may be attributed to presence of more Nb element solid solution in Zr-1Nb matrix [39,40]. Correspondingly, Zr-0.35Nb has larger elongations at both room temperature (14%) and 380 °C (22.4%) than Zr-1Nb (12% at room temperature and 20.9% at 380 °C).

Table 2
Mechanical properties of alloys in air at room temperature and 380 °C. UTS indicates ultimate tensile strength. Scatter bands represent the standard deviations of three independent samples.

Alloy	Room temperature		380 °C	
	UTS (MPa)	Elongation (%)	UTS (MPa)	Elongation (%)
Zr-0.35Nb	590 ± 5	14.0 ± 1.5	381 ± 5	22.4 ± 0.3
Zr-1Nb	698 ± 19	12.0 ± 0.9	447 ± 27	20.9 ± 1

3.3. Microstructures of alloys near the interface of the oxide/metal after 100-day exposure

Fig. 4 shows the microstructures of the alloys near the interface of the oxide/metal after 100-day exposure. Recrystallized grains with sizes of 0.5–2 μm are observed near the oxide/metal interface, associated with precipitated SPPs (Fig. 4a and c), both for Zr-0.35Nb and Zr-1Nb. Such microstructures are significantly different from those observed after final annealing (Fig. 2c and d). In Zr-0.35Nb, the SPPs are merely 10–20 nm in diameter and their volume fraction is about 2.9% (Fig. 4a). As shown by the white square in Fig. 4a, the SPPs are identified as C15 type face-centered structured (Zr, Nb)Fe_2 particles by Fast Fourier Transform (Fig. 4b). The same phenomenon is revealed in Zr-1Nb; the location in the vicinity of the interface (location A) contains more SPPs (about 12.3 vol.%) than that slightly further away from the interface (location B, about 7.1 vol.%) (Fig. 4c). Most SPPs in Zr-1Nb are identified as C14 type hexagonal structured Zr(Nb, $Fe)_2$ (Fig. 4d). It is worth noting that the SPPs in both samples would be capsuled by the oxides as corrosion progresses.

3.4. Nanoscratch tests

Fig. 5 illustrates the relationship between penetration depth/acoustic emission and normal force/displacement of the Zr-0.35Nb-3 and Zr-1Nb-3 specimens. In the figure, PD stands for the penetration depth curve and AE means acoustic emission curve. The images below the curves show the corresponding scratch tracks. A–H are the magnified images as indicated by the red dash rectangles in Fig. 5a and b. The peaks of the acoustic emission curve are associated with the detection of flaws (such as cracks) in the oxides and the size of a flaw is always proportional to the intensity of the peak of the acoustic emissions [31]. The magnified images were selected on basis of the peak positions of the acoustic emission curves. If there were not sufficient peaks to be chosen, random selection was conducted. As seen from Fig. 5a, the penetration depth increases linearly with the increase of the normal force. Only a strong peak of acoustic emissions is detected. Meanwhile, only a few tiny cracks are found in the scratch tracks and the oxides are still attached to the substrate after 10 N load for Zr-0.35Nb-3 (Fig. 5a-B, C, D). The bare metal is hardly observed in Fig. 5a-C and disappears in Fig. 5a-D. This result indicates that the thickness of the oxide layer is inhomogeneous due to the undulations of the oxide/metal interface, which has been reported elsewhere [13,26,27]. In contrast, the bare metal is presented at the load of about 7 N for Zr-1Nb-3 (Fig. 5b). The number of cracks in the scratch track for Zr-1Nb-3 is greater than that for Zr-0.35Nb-3 (Figs. 5b-E, F, G). Meanwhile, the number of acoustic emission peaks for Zr-1Nb-3 is also greater than that for Zr-0.35Nb-3.

The slopes of the penetration depth curves could be regarded as a qualitative method to evaluate the hardness of the oxides. The lower the slope of the penetration depth curve, the more difficult the indenter penetrates the oxides. Since the penetration depth curves always consist of several segments (such as an oxide segment and a metal segment), fitting is not a convenient way to calculate the slopes. In this work, therefore, the slopes of the penetration depth curves are evaluated by drawing a line approaching the curve within the oxide segment scale and then calculating the slope of this line. As seen from Fig. 5, the slopes of the penetration depth curves are 117 nm/N for Zr-0.35Nb-3 and 165 nm/N for Zr-1Nb-3, indicating that the oxides formed on Zr-0.35Nb-3 in 0.01 M LiOH aqueous solution at 360 °C/18.6 MPa are harder than those formed on Zr-1Nb-3.

The same analyses could be applied to Fig. 6, which represents the results of nanoscratch tests for Zr-0.35Nb-42 and Zr-1Nb-42. As the thickness of the oxides increases, the oxides on both alloys are still attached to their substrate after 10 N load. However, bare metal can be found continuously at about 1.8 μm depth in the scratch track for Zr-

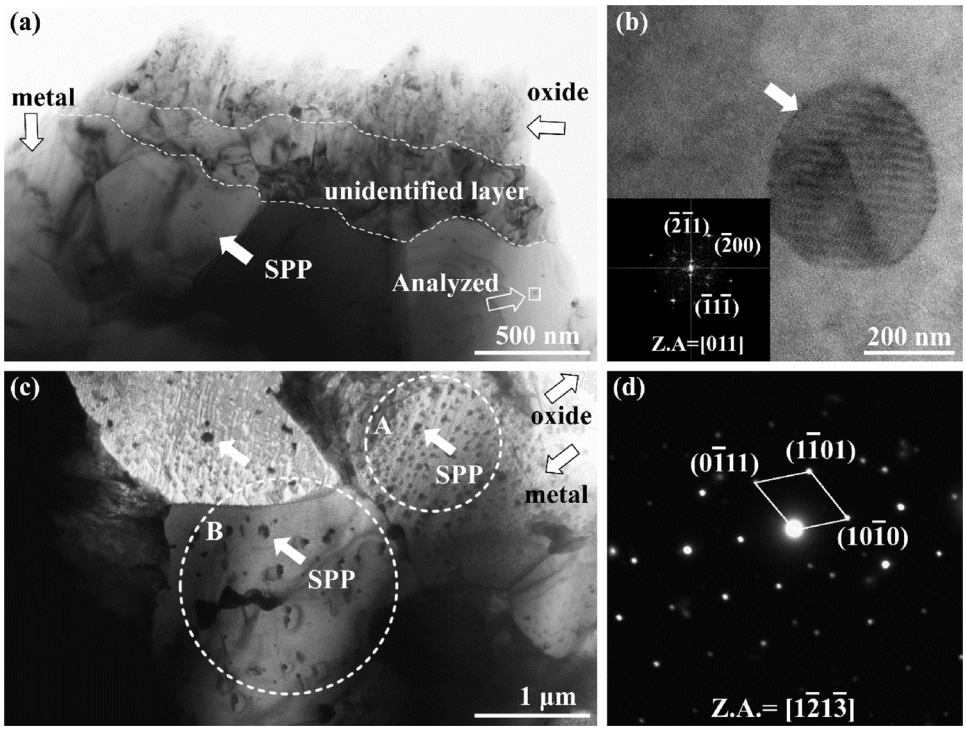

Fig. 4. TEM micrographs showing the oxide/metal interfaces for Zr-0.35Nb and Zr-1Nb in 0.01 M LiOH aqueous solution at 360 °C/18.6 MPa for 100-day exposure: (a) Zr-0.35Nb, recrystallized grains associated with precipitated second-phase particles (SPPs) are observed; (b) high resolution image as indicated by white square in (a), the inset is the Fast Fourier Transform for the SPP (identified as C15 type (Zr, Nb)Fe_2 particle) in (b); (c) Zr-1Nb, recrystallized grains associated with multiple SPPs are observed; and (d) selected area electron diffraction pattern for SPPs (identified as C14 type hexagonal structured Zr $(Nb, Fe)_2$ particle) in (c). Z.A. is the zone axis.

1Nb-42 (Fig. 6b-G), resulting in a broad peak of the acoustic emission curve in Fig. 6b. Regardless of the other scratch information, it is worth noting that the penetration depths are still in proportion to the normal force before the indenters penetrate the metal substrate, indicating that the oxides formed on Zr-0.35Nb and Zr-1Nb after 42-day exposure in 0.01 M LiOH aqueous solution at 360 °C/18.6 MPa are still homogeneous. The slope of the penetration depth curve of Zr-0.35Nb-42 is 168 nm/N, which is smaller than that of Zr-0.1Nb-42 (201 nm/N).

Fig. 7 shows the nanoscratch results for Zr-0.35Nb-100 and Zr-1Nb-100. As mentioned in Section 3.1, the transition in corrosion kinetics of Zr-1Nb takes place after 100-day exposure. It has been reported that a lot of lateral cracks would be present in the oxides formed on zirconium alloys at high temperature in water or aqueous solutions and the outer layers of the corresponding oxides would become loose and porous at this period [13,25–27,41]. The slopes of the penetration depth curves for both samples change at a certain depth (as indicated by segment 1 and 2 in Fig. 7). This represents the formation of the two layers of the oxides with different hardness after 100-day exposure. Both slopes of the penetration depth curves in segment 1 (335 nm/N for Zr-0.35Nb-100 and 528 nm/N for Zr-1Nb-100) are larger than the corresponding ones in segment 2 (177 nm/N for Zr-0.35Nb-100 and 258 nm/N for Zr-1Nb-100), indicating that the inner layers of the oxides are more compact and harder than the outer layers of the oxides. Furthermore, a bunch of the acoustic emission peaks are observed in Fig. 7b. These peaks correspond to large cracks in the oxides or the interface of the oxide/metal, as indicating in Fig. 7b-F, G, H. Furthermore, the indenter penetrates the metal substrate at about 7 N normal force load for Zr-1Nb-100.

The nanoscratch results for Zr-0.35Nb-130 and Zr-1Nb-130 are presented in Fig. 8. Two segments of the penetration depth curves are still observed in both samples. The slopes in segment 1 are 496 nm/N for Zr-0.35Nb-130 and 722 nm/N for Zr-1Nb-130. The slopes in segment 2 are 242 nm/N for Zr-0.35Nb-130 and 364 nm/N for Zr-1Nb-130. The penetration depth curve of Zr-1Nb-130 has a sharp fluctuation,

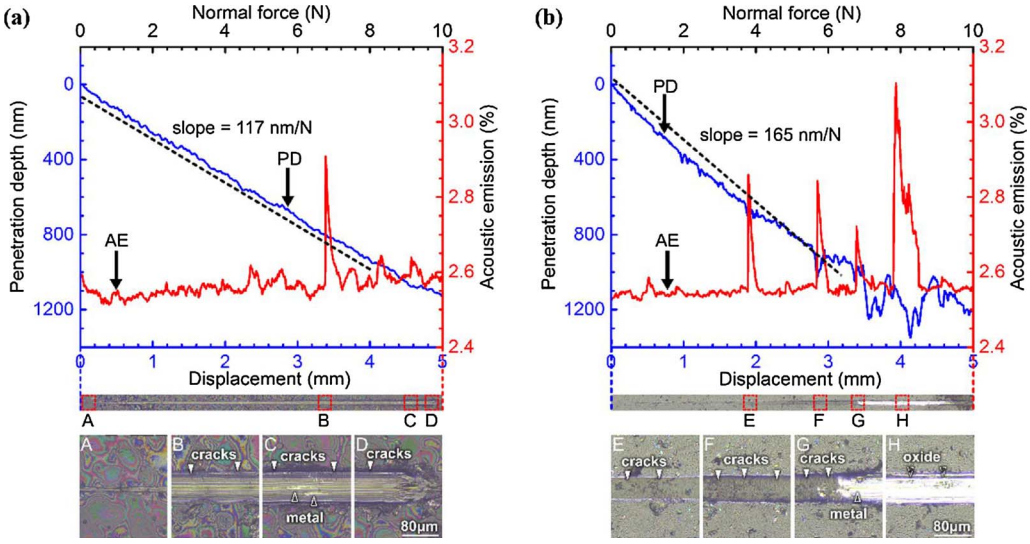

Fig. 5. Penetration depth and acoustic emission as a function of scratch load and displacement of specimen for (a) Zr-0.35Nb-3 and (b) Zr-1Nb-3. The images below each curve are the corresponding scratch tracks. A–H are the magnified images as indicated by the red dash rectangles in (a) and (b). Only one strong acoustic emission peak is detected and a few tiny cracks are found in the scratch track for Zr-0.35Nb-3. In contrast, the bare metal is presented at the load of about 7 N for Zr-1Nb-3 and more cracks are found in the scratch track for Zr-1Nb-3. The slopes of the penetration depth curves are 117 nm/N for Zr-0.35Nb-3 and 165 nm/N for Zr-1Nb-3, indicating that the oxides formed on Zr-0.35Nb-3 is harder than those formed on Zr-1Nb-3.

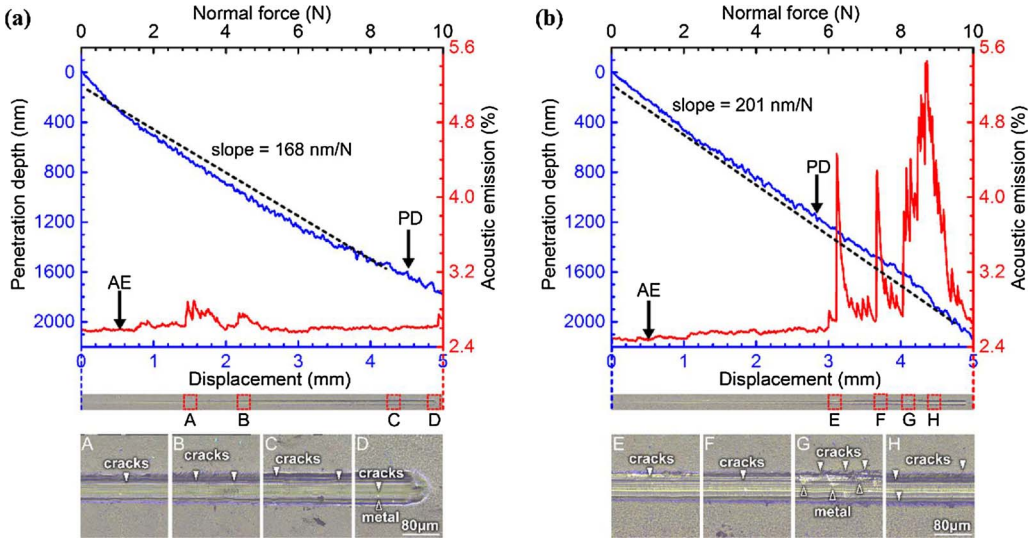

Fig. 6. Penetration depth and acoustic emission as a function of scratch load and displacement of specimen for (a) Zr-0.35Nb-42 and (b) Zr-1Nb-42. The images below each curve are the corresponding scratch tracks. A–H are the magnified images as indicated by the red dash rectangles in (a) and (b). A few tiny cracks are found in the scratch track for Zr-0.35Nb-42. In contrast, more cracks are observed in the scratch track for Zr-1Nb-42. A broad peak of the acoustic emission curve in Fig. 6(b) coincides with the depth located at the interface of the oxide/metal for Zr-1Nb-42 (Figs. 6b-G and H). The slope of the penetration depth curve for Zr-0.35Nb-42 is 168 nm/N, which is smaller than that for Zr-0.1Nb-42 (201 nm/N) (For interpretation of the references to color in this figure legend, the reader is referred to the web version of this article.).

corresponding to the depth of about 2.4 μm (Fig. 8b). At this location, plenty of cracks are noted (Fig. 8b-E). By SEM examination, the delamination of the oxide layer is found (Fig. 8b inset), indicating that the Zr-1Nb has undergone the transition in corrosion kinetics. This phenomenon is always associated with long linked-up cracks as reported in previous research [15,21–23,27,42], which could be the main reason accounting for the sharp fluctuation of the penetration depth curve in Fig. 8b. Indenters penetrate the metal substrate at approximately 10 N load for Zr-0.35Nb-130 and Zr-1Nb-130.

4. Discussion

4.1. Formation of the microstructures before and after corrosion

In this work, the alloy samples underwent the second β-quenching at 1050 °C, then were cold-rolled twice to the final thickness accompanied by intermediate annealing of 470 °C and final annealing of 470 °C. Typically, the alloying elements would dissolve into the matrix when alloys were annealed at β-Zr region [11,43]. After the second β-quenching, alloying elements were still in solid solution in the matrix. Recent work [33,44] suggested that migration energy of Nb^{5+} and activation energy of Nb-containing SPPs are much greater than the corresponding values for Zr^{4+} and Nb-free SPPs in zirconium alloys. Therefore, the precipitation of SPPs becomes difficult after the second β-quenching [33,45]. Meanwhile, the recrystallization is also sluggish and the lath structures formed by β → α transformation in both alloys are retained. The solid solubility of Nb is no more than 0.3% in α-Zr at phase equilibrium at room temperature [46]. Therefore, 0.35% Nb oversaturated in α-Zr is in a non-equilibrium state for Zr-0.35Nb after the final annealing. Compared to Zr-0.35Nb, Zr-1Nb contains more Nb element. Although the same processing procedure is conducted on Zr-1Nb, some fine SPPs still precipitate (Fig. 2b). However, the fraction of SPPs (0.2 vol.%) in Zr-1Nb is much lower than the fraction of SPPs in the alloys with the same or similar chemical compositions [34,47,48]. Thus, there is still considerable Nb solid solution in the matrix for Zr-1Nb.

When zirconium alloys are corroded in aqueous solutions under conditions of high temperature and high pressure, the inward diffusion of oxide ions leads to the continuous growth of oxides [49]. These oxide ions even penetrate the matrix during corrosion [50,51]. Meanwhile, due to the large volume difference between Zr and ZrO_2 (1:1.56), mechanical stress is produced at the oxide/metal interface, leading to the movement of dislocations in the metal substrate during the corrosion test [52]. As discussed above, the microstructures of the alloy samples after final annealing are oversaturated and partially recrystallized. Therefore, one can speculate that some changes occur in the matrix under the combined effect of inward diffusion of oxide ions and mechanical stress when alloys are corroded in LiOH aqueous solution at

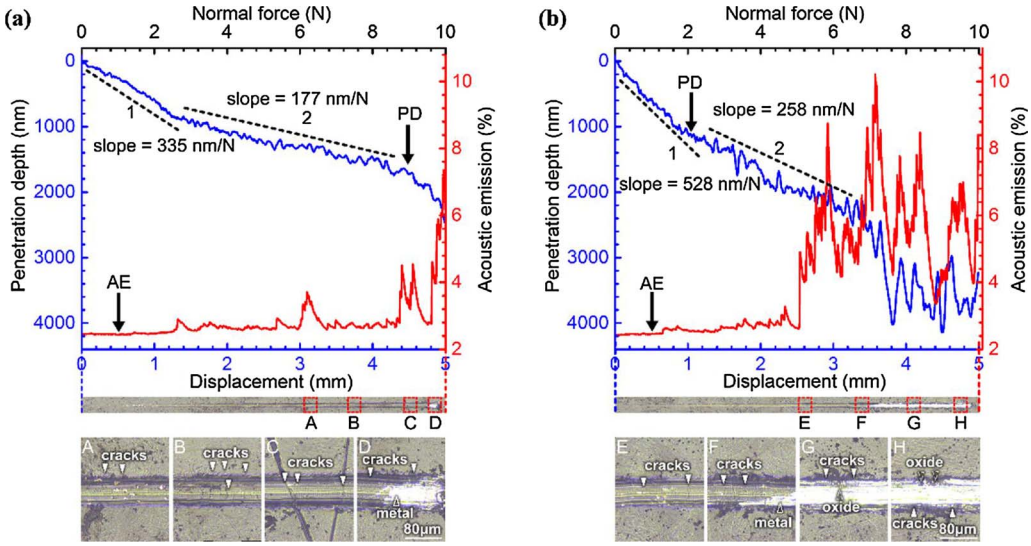

Fig. 7. Penetration depth and acoustic emission as a function of scratch load and displacement of specimen for (a) Zr-0.35Nb-100 and (b) Zr-1Nb-100. The images below each curve are the corresponding scratch tracks. A–H are the magnified images as indicated by the red dash rectangles in (a) and (b). More and stronger acoustic emission peaks are detected for Zr-0.35Nb-100 and Zr-1Nb-100. Both slopes of the penetration depth curves in segment 1 (335 nm/N for Zr-0.35Nb-100 and 528 nm/N for Zr-1Nb-100) are larger than the corresponding ones in segment 2 (177 nm/N for Zr-0.35Nb-100 and 258 nm/N for Zr-1Nb-100) (For interpretation of the references to color in this figure legend, the reader is referred to the web version of this article.).

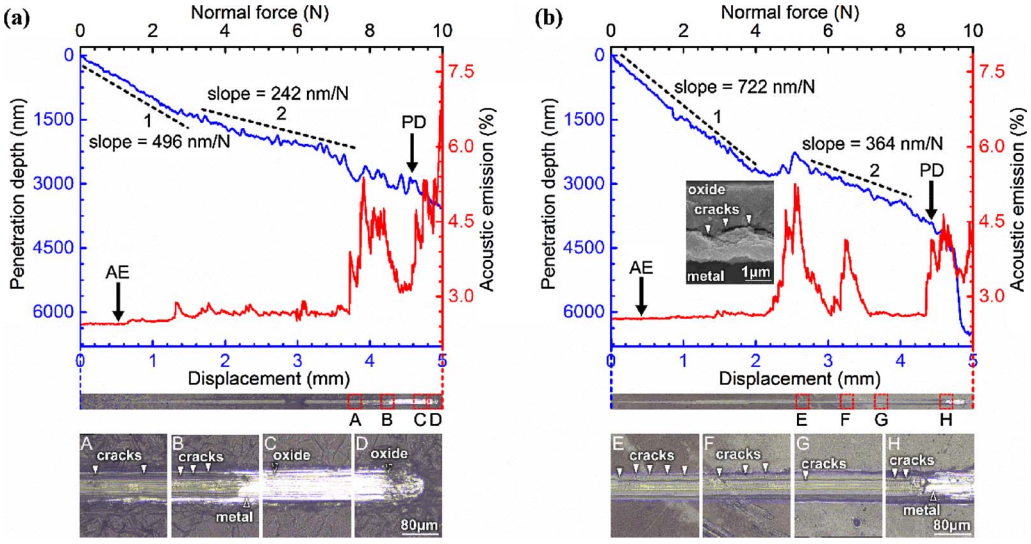

Fig. 8. Penetration depth and acoustic emission as a function of scratch load and displacement for (a) Zr-0.35Nb-130 and (b) Zr-1Nb-130. The images below each curve are the corresponding scratch tracks. A–H are the magnified images as indicated by the red dash rectangles in (a) and (b). The slopes of the penetration depth curves in segment 1 are 496 nm/N for Zr-0.35Nb-130 and 722 nm/N for Zr-1Nb-130, larger than those in segment 2 (242 nm/N for Zr-0.35Nb-130 and 364 nm/N for Zr-1Nb-130). A sharp fluctuation is observed in the penetration depth curve for Zr-1Nb-130, corresponding to the delamination of the oxide layer (the inset SEM image for cross-sectional oxide in (b)) located at the depth of about 2.4 μm (For interpretation of the references to color in this figure legend, the reader is referred to the web version of this article.).

360 °C/18.6 MPa for an extended period. Saintoyant et al. [53] proposed that recrystallization could take place at a relatively low temperature if a stress is applied. As shown in Fig. 2c and d, the alloy samples have lath structures with a large number of dislocations. After being corroded at 360 °C and chronically stressed, recrystallization in the vicinity of the oxide/metal interface takes place in both Zr-0.35Nb and Zr-1Nb. Thus, precipitates of SPPs are observed in the region adjacent to the oxide/metal interfaces in both Zr-0.35Nb-100 and Zr-1Nb-100 (Fig. 4). Comparatively, Zr-0.35Nb-100 has fewer (2.9 vol.%) and smaller (10–20 nm) SPPs in the region nearby the interface of the oxide/metal since Zr-0.35Nb possesses a lower content of Nb elements.

4.2. Strengths of the substrates vs. properties of the oxides

Many studies reported that the deformation of the Zr substrate during corrosion in water or aqueous solutions under conditions of high temperature and high pressure led to a redistribution of stress in the oxides, then the cracks were triggered [13,22,23,41]. Thus, the alloy strength has been considered as an important influencing factor for the transition in corrosion kinetics, and the higher strength alloys may often have longer pre-transition times [11,13,22,23]. These results might be suitable for alloys with the identical compositions [21,22]. However, this law does not seem to apply to Zr-0.35Nb and Zr-1Nb (Fig. 3 and Table 2). Based on the requirements for the formation of cracks in the oxides, not only the redistribution of stress induced by the deformation of the substrate but also other factors such as the properties of the oxides should be considered.

As seen from Fig. 4, more SPPs are incorporated into the oxides in Zr-1Nb since Zr-1Nb contains more Nb elements. Moreover, the C14 type SPPs in zirconium alloys are oxidized more slowly than the surrounding matrix in aqueous solutions at high temperature [29]. Thus, the C14 type SPPs are prone to induce micro-cracks in the oxides [54]. As a result, more peaks of acoustic emissions, caused by flaws (such as micro-cracks), are detected in nanoscratch tests for Zr-1Nb (Figs. 5b, 6b, 7b and 8b). This demonstrates that the oxides formed on Zr-1Nb are more susceptible to the formation of micro-cracks in another way. Meanwhile, from the perspective of the slopes of the penetration depth curves (Figs. 5–8), the oxides formed on Zr-1Nb in 0.01 M LiOH aqueous solution at 360 °C/18.6 MPa within 130-day exposure have a lower hardness compared to the oxides formed on Zr-0.35Nb. In general, cracks are triggered by stress [41,54]. As such, cracks are more prone to occur in the oxides formed on Zr-1Nb in this work. Hence, the transition in corrosion kinetics of Zr-1Nb associated with the delamination of the oxides is detected earlier than that of Zr-0.35Nb (Figs. 3 and 8).

4.3. Degradation of the oxides

The oxides formed on Zr-0.35Nb and Zr-1Nb in 0.01 M LiOH aqueous solution at 360 °C/18.6 MPa at 3-day and 42-day exposure are still relatively homogeneous (Figs. 5 and 6). However, as the exposure time is extended, two segments of the penetration depth curves with different slopes are found in Zr-0.35Nb and Zr-1Nb at 100-day and 130-day exposure (Figs. 7 and 8). The slopes of segment 1 of the penetration depth curves are larger than those of segment 2 for both Zr-0.35Nb and Zr-1Nb (Figs. 7 and 8). It is known that the compressive stress decreases as the thickness of the oxide layers increases [55]. The relaxation of stress is believed to be an important factor for the degradation of the oxides [27]. Zr-1Nb does not show any apparent sign of the transition in LiOH aqueous solution at 360 °C/18.6 MPa under 100-day exposure (Fig. 3) but the penetration depth curve for Zr-1Nb-100 displays two segments (Fig. 7b), indicating that the outer oxide layer of Zr-1Nb-100 degrades before the transition in corrosion kinetics. This result suggests that the outer oxide layer becomes loose and the inner oxide layer is still compact, although the oxides have not substantially delaminated.

Another interesting phenomenon is that the thickness of the loose oxide layer seems to become greater as corrosion progresses (segment 1 in Figs. 7 and 8). The thickness of the compact oxide layer is kept at a relatively constant level of about 1–1.2 μm before the transition in corrosion kinetics (segment 2 in Figs. 7a, b and 8a). If the loosening process in the oxides gradually takes place as the in-plane stress gradually relaxes far away from the interface of the oxide/metal [55–57], two segments of the penetration depth curves would not be observed as the exposure time increases. Although there is still a lack of sufficient evidence to interpret the exact reason for the formation of two segments on the penetration depth curves, some facts can be deduced from the growth characteristics of the oxides. The region in the oxide near the oxide/metal interface is subjected to large compressive stress due to the volume difference between Zr and ZrO_2 [41]. Two segments on the penetration depth curves for Zr-0.35Nb and Zr-1Nb are presented when the thicknesses of the oxides exceed a certain value (Figs. 7 and 8). This apparent change in the slopes of the penetration depth curves may be ascribed to the transformation of monoclinic ZrO_2 grains from tetragonal ZrO_2 grains which could be stabilized by compressive stress [58]. This phase transformation would induce flaws (such as pores and micro-cracks) into the local region of the oxides formed on zirconium alloys in water or aqueous solutions under conditions of high temperature and high pressure [58,59]. The compressive stress decreases gradually from the interface of the oxide/metal to the surface of the oxides [55,57]. Hence, the compressive stress would reduce to a level at a distance from the interface of the oxide/metal and could not stabilize

the tetragonal ZrO_2 grains. A considerable number of tetragonal ZrO_2 grains transform to monoclinic ZrO_2 grains at a certain distance from the oxide/metal interface. Therefore, the oxides degrade quickly far away from the oxide/metal interface. As such, two slopes of the penetration depth curves are evident.

4.4. Possible mechanism relating to the transition in corrosion kinetics

The delamination of oxides is widely proved as indicative of the transition in corrosion kinetics which initially results from the formation of lateral cracks in oxides formed on zirconium alloys in water or aqueous solutions under conditions of high temperature and high pressure [21–23]. In such a corrosion environment, the reason for oxide delamination is attributed to the combined effect of the deformation of the metal substrate and the production of cracks in the oxides. Although the redistribution of stress in oxides mainly stems from the deformation of the substrate [22,41,60], the formation of cracks definitively depends on the properties of oxides. Special attention should be paid to the distinctive properties of oxides due to the different compositions and microstructures of zirconium alloys. In the present work, the corrosion test in autoclave was performed in an aqueous environment at 360 °C/18.6 MPa. This corresponds to the alloys being aged for an extended period at 360 °C. In the meantime, the substrate is subjected to tensile stress near the oxide/metal interface chronically. Therefore, as seen from a schematic illustration in Fig. 9a, the non-equilibrium microstructures of zirconium alloys might vary under conditions of high temperature and high pressure and the properties of the oxides would be determined in terms of the altered microstructures, as Zr-0.35Nb and Zr-1Nb in this work. In comparison, the equilibrium microstructure (such as recrystallized microstructure) of zirconium alloys may not much change (Fig. 9b) [52].

5. Conclusions

Two non-equilibrium Zr-Sn-Nb-Fe-Cu-O alloys with different Nb contents, i.e. Zr-0.4Sn–0.35Nb-0.3Fe-0.05Cu-0.08O (denoted as Zr-0.35Nb) and Zr-0.4Sn-1Nb-0.3Fe-0.05Cu-0.08O (denoted as Zr-1Nb), were corroded in 0.01 M LiOH aqueous solution at 360 °C. The corrosion behavior of the alloys and the degradation of the surface oxide films were investigated by transmission electron microscope and nanoscratch tests. Some key conclusions can be drawn as follows:

1 Although Zr-0.35Nb and Zr-1Nb have similar microstructures prior to corrosion test, they exhibit significantly different corrosion behavior within the testing period. The transition in corrosion kinetics for Zr-1Nb takes place after 100-day exposure, whereas Zr-0.35Nb shows no apparent sign of the transition with up to 200-day exposure.
2 After an extended period corroded at 360 °C, local recrystallization of the Zr matrix and precipitates of second-phase particles are observed near the oxide/metal interface in both alloys. More second-phase particles are found in Zr-1Nb than in Zr-0.35Nb, which is attributed to higher Nb content in Zr-1Nb. These second-phase particles would be incorporated into the oxides as corrosion proceeds.
3 By comparing the nanoscratch results obtained on the oxides formed the alloys at the same exposure time, the oxides formed on Zr-0.35Nb show a higher hardness and fewer flaws than those formed on Zr-1Nb. Therefore, the oxides formed on Zr-1Nb break down earlier than those formed on Zr-0.35Nb. This may stem from the different amounts of second-phase particles embedded in the oxides formed on both alloys.
4 According to the penetration depth curves obtained on the oxides formed on the alloys at different exposure time, the oxides degrade gradually as corrosion progresses. After 100-days exposure, the outer oxide layers show a lower hardness than the inner oxide layers

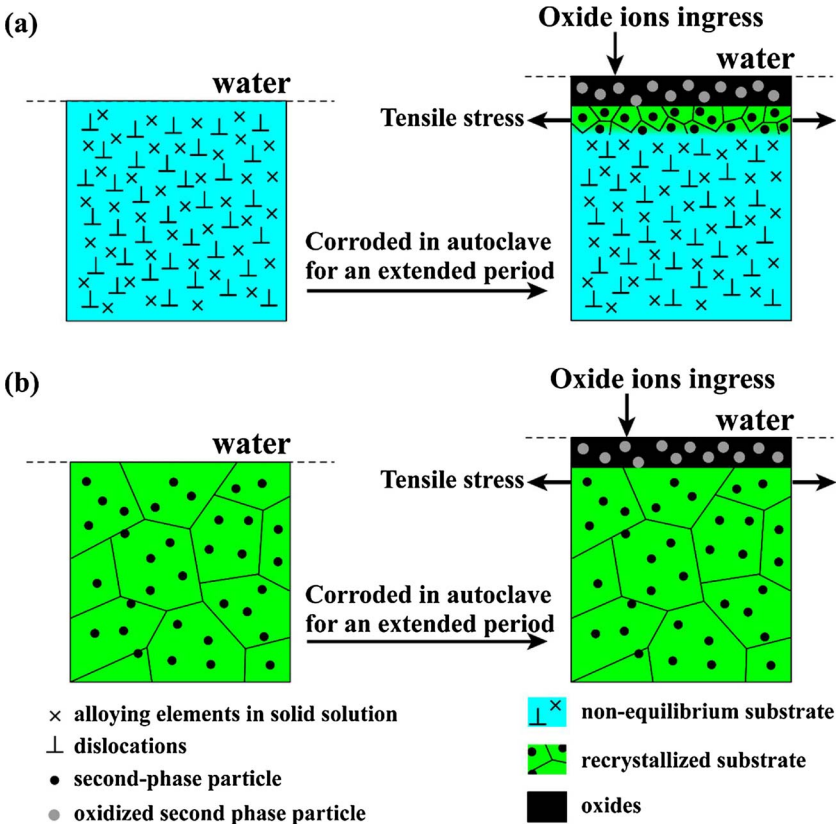

Fig. 9. Schematic illustrations for the possible mechanism of zirconium alloys with non-equilibrium and equilibrium microstructures in water or aqueous solutions at 360 °C/18.6 MPa for an extended period: (a) The non-equilibrium microstructures of zirconium alloys might vary under these conditions and the properties of the oxides would be determined in terms of the altered microstructure, (b) the equilibrium microstructures of zirconium alloys may not change much.

for both Zr-0.35Nb and Zr-1Nb, even though the transition in corrosion kinetics does not take place in the two alloys.

This work suggests that the variations of non-equilibrium microstructures significantly influence the properties of the oxides grown from the metal substrates, thereby determining the corrosion performance of the Zr alloys.

Acknowledgements

The authors would like to acknowledge the financial support provided by the National Natural Science Foundation (51601075), the China Postdoctoral Science Foundation Funded Project (2017M611751), the Natural Science Foundation of Hebei Province of China (E2015203250) and the Young Teachers Program of Yanshan University (14LGA005), and Jiangsu University of Science and Technology Overseas Research & Training Program for University Prominent Young & Middle-aged Teachers.

References

[1] C.M. Lee, D.S. Sohn, Enhanced high-temperature oxidation resistance of a zirconium alloy cladding by high-temperature preformed oxide on the cladding, Corros. Sci. 131 (2018) 116–125.
[2] P. Platt, D. Lunt, E. Polatidis, M.R. Wenman, M. Preuss, In-situ digital image correlation for fracture analysis of oxides formed on zirconium alloys, Corros. Sci. 111 (2016) 344–351.
[3] T. Kim, J. Kim, K.J. Choi, S.C. Yoo, S. Kim, J.H. Kim, Phase transformation of oxide film in zirconium alloy in high temperature hydrogenated water, Corros. Sci. 99 (2015) 134–144.
[4] L. Chen, J. Li, Y. Zhang, L.C. Zhang, W. Lu, L. Wang, L. Zhang, D. Zhang, Zr–Sn–Nb–Fe–Si–O alloy for fuel cladding candidate: processing, microstructure, corrosion resistance and tensile behavior, Corros. Sci. 100 (2015) 332–340.
[5] J. Zhang, Y. Hu, J. Huang, L. Tu, M. Yao, B. Zhou, The corrosion resistance of Zr-0.7Sn-1Nb-0.2Fe-xCu-xGe alloys in 360 °C lithiated water, Corros. Sci. 111 (2016) 132–138.
[6] A. Couet, A.T. Motta, A. Ambard, D. Livigni, In-situ electrochemical impedance spectroscopy measurements of zirconium alloy oxide conductivity: relationship to hydrogen pickup, Corros. Sci. 119 (2017) 1–13.
[7] Z. Wang, B.X. Zhou, B. Chen, W. Zhu, B. Wen, L. Wu, H.K. Tang, Z.Q. Fang, Q. Li, M.Y. Yao, In-situ oxidation and short-time corrosion investigation on strain and dislocation during the generation and growth of ZrO_2, Corros. Sci. 122 (2017) 26–31.
[8] B.D.C. Bell, S.T. Murphy, P.A. Burr, R.J. Comstock, J.M. Partezana, R.W. Grimes, M.R. Wenman, The influence of alloying elements on the corrosion of Zr alloys, Corros. Sci. 105 (2016) 36–43.
[9] A. Garner, J. Hu, A. Harte, P. Frankel, C. Grovenor, S. Lozano-Perez, M. Preuss, The effect of Sn concentration on oxide texture and microstructure formation in zirconium alloys, Acta Mater. 99 (2015) 259–272.
[10] J. Wei, P. Frankel, E. Polatidis, M. Blat, A. Ambard, R.J. Comstock, L. Hallstadius, D. Hudson, G.D.W. Smith, C.R.M. Grovenor, The effect of Sn on autoclave corrosion performance and corrosion mechanisms in Zr–Sn–Nb alloys, Acta Mater. 61 (2013) 4200–4214.
[11] L. Chen, Q. Zeng, J. Li, J. Lu, Y. Zhang, L.C. Zhang, X. Qin, W. Lu, L. Zhang, L. Wang, Effect of microstructure on corrosion behavior of a Zr–Sn–Nb–Fe–Cu–O alloy, Mater. Des. 92 (2016) 888–896.
[12] A. Garner, P. Frankel, J. Partezana, M. Preuss, The effect of substrate texture and oxidation temperature on oxide texture development in zirconium alloys, J. Nucl. Mater. 484 (2017) 347–356.
[13] L. Chen, J. Li, Y. Zhang, L.C. Zhang, W. Lu, L. Zhang, L. Wang, D. Zhang, Effects of alloyed Si on the autoclave corrosion performance and periodic corrosion kinetics in Zr–Sn–Nb–Fe–O alloys, Corros. Sci. 100 (2015) 651–662.
[14] B.D.C. Bell, S.T. Murphy, P.A. Burr, R.W. Grimes, M.R. Wenman, Accommodation of tin in tetragonal ZrO_2, J. Appl. Phys. 117 (2015) 084901.
[15] W. Gong, H. Zhang, C. Wu, H. Tian, X. Wang, The role of alloying elements in the initiation of nanoscale porosity in oxide films formed on zirconium alloys, Corros. Sci. 77 (2013) 391–396.
[16] J. Hu, L. Yang, G. Cao, Y. Yun, G. Yuan, Q. Yue, G. Shao, On the oxidation behavior of $(Zr,Nb)_2Fe$ under simulated nuclear reactor conditions, Corros. Sci. 112 (2016) 718–723.
[17] B.D.C. Bell, S.T. Murphy, R.W. Grimes, M.R. Wenman, The effect of Nb on the corrosion and hydrogen pick-up of Zr alloys, Acta Mater. 132 (2017) 425–431.
[18] J. Huang, M. Yao, B. Chen, Y. Mao, X. Liang, J. Zhang, B. Zhou, Q. Li, Oxidation behavior of Zr_9S_2 precipitates in Zr-0.8Sn-1.0Nb-0.3Fe-0.1Cr-xS alloys, Corros. Sci. 120 (2017) 82–89.
[19] J. Huang, M.Y. Yao, C.Y. Gao, P.F. Hu, X. Liang, J.L. Zhang, B.X. Zhou, Q. Li, E. Ahsan, Analysis of the oxidized surface of 90Nb-10Zr alloy after exposure to lithiated water with 0.01 M LiOH at 360 °C/18.6 MPa, Corros. Sci. 104 (2016) 269–276.
[20] J. Škarohlíd, P. Ashcheulov, R. Škoda, A. Taylor, R. Čtvrtlík, J. Tomáštík, F. Fendrych, J. Kopeček, V. Cháb, S. Cichoň, P. Sajdl, J. Macák, P. Xu, J.M. Partezana, J. Lorinčík, J. Prehradná, M. Steinbrück, I. Kratochvílová, Nanocrystalline diamond protects Zr cladding surface against oxygen and hydrogen uptake: Nuclear fuel durability enhancement, Sci. Rep. 7 (2017) 1–14.
[21] A. Ly, A. Ambard, M. Blat-Yrieix, L. Legras, P. Frankel, M. Preuss, C. Curfs, G. Parry, Y. Bréchet, Understanding crack formation at the metal/oxide interface during corrosion of Zircaloy-4 using a simple mechanical model, J. ASTM Int. 8 (2011) 1–29.
[22] V. Likhanskii, T.N. Aliev, M.Y. Kolesnik, I.A. Evdokimov, V.G. Zborovskii, Method of elastic energy minimization for evaluation of transition parameters in oxidation kinetics of Zr alloys, Corros. Sci. 61 (2012) 143–147.
[23] V. Likhanskii, M. Kolesnik, On the evolution of wave structure at the metal/oxide interface during oxidation of Zr alloys, Corros. Sci. 87 (2014) 416–420.
[24] J.Y. Park, B.K. Choi, S.J. Yoo, Y.H. Jeong, Corrosion and oxide properties of HANA alloys, J. ASTM Int. 5 (2008) 471–485.
[25] N. Ni, S. Lozano-Perez, M.L. Jenkins, C. English, G.D.W. Smith, J.M. Sykes, C.R.M. Grovenor, Porosity in oxides on zirconium fuel cladding alloys, and its importance in controlling oxidation rates, Scr. Mater. 62 (2010) 564–567.
[26] W. Gong, H. Zhang, Y. Qiao, H. Tian, X. Ni, Z. Li, X. Wang, Grain morphology and crystal structure of pre-transition oxides formed on Zircaloy-4, Corros. Sci. 74 (2013) 323–331.
[27] N. Ni, S. Lozanoperez, J.M. Sykes, G.D. Smith, C.R.M. Grovenor, Focussed ion beam sectioning for the 3D characterisation of cracking in oxide scales formed on commercial ZIRLO™ alloys during corrosion in high temperature pressurised water, Corros. Sci. 53 (2011) 4073–4083.
[28] J. Huang, M.Y. Yao, C.Y. Gao, X. Liang, J.C. Peng, J.L. Zhang, B.X. Zhou, The influence of second-phase particles on the crack formation in oxide films formed on zirconium alloys, Corros. Sci. 99 (2015) 172–177.
[29] J.C. Caldwell, P. Caldwell, Oxidation behaviour of zirconium alloys and their precipitates – a mechanistic study, J. Nucl. Mater. 432 (2013) 222–238.
[30] W. Conshohocken, Standard test method for corrosion testing of products of zirconium, hafnium, and their alloys in water at 680 °F or in steam at 750 °F, Test 88 (2002) 1–8.
[31] C.R. Heiple, S.H. Carpenter, Acoustic emission produced by deformation of metals and alloys-a review, J. Acoust. Emiss. 6 (1987) 177–204.
[32] W.K. Wang, H.C. Wen, C.H. Cheng, C.H. Hung, W.C. Chou, W.H. Yau, P.F. Yang, Y.S. Lai, Nanotribological properties of ALD-processed bilayer TiO_2/ZnO films, Microelectron. Reliab. 54 (2014) 2754–2759.
[33] B.F. Luan, L.J. Chai, J.W. Chen, M. Zhang, Q. Liu, Growth behavior study of second phase particles in a Zr–Sn–Nb–Fe–Cr–Cu alloy, J. Nucl. Mater. 423 (2012) 127–131.
[34] H. Yang, J. Shen, Y. Matsukawa, Y. Satoh, S. Kano, Z. Zhao, Y. Li, F. Li, H. Abe, Effects of alloying elements (Sn, Nb, Cr, and Mo) on the microstructure and mechanical properties of zirconium alloys, J. Nucl. Sci. Technol. 52 (2015) 1162–1173.
[35] L. Chai, H. Wu, S. Wang, K. Chen, T. Wang, J. Xia, Characterization of microstructure and hardness of a Zr-2.5Nb alloy surface-treated by pulsed laser, Mater. Chem. Phys. 198 (2017) 303–309.
[36] Y. Chen, J. Zhang, N. Dai, P. Qin, H. Attar, L.C. Zhang, Corrosion behaviour of selective laser melted Ti-TiB biocomposite in simulated body fluid, Electrochim. Acta 232 (2017) 89–97.
[37] H.B. Lu, L.C. Zhang, A. Gebert, L. Schultz, Pitting corrosion of Cu–Zr metallic glasses in hydrochloric acid solutions, J. Alloy Compd. 462 (2008) 60–67.
[38] X. Qin, X. Guo, J. Lu, L. Chen, J. Qin, W. Lu, Erosion-wear and intergranular corrosion resistance properties of AISI 304L austenitic stainless steel after low-temperature plasma nitriding, J. Alloy Compd. 698 (2016) 1094–1101.
[39] H.L. Yang, S. Kano, Y. Matsukawa, Y.F. Li, J.J. Shen, F. Li, Z.S. Zhao, Y. Satoh, H. Abe, Effect of molybdenum on microstructures in Zr-1.2Nb alloys after β-quenching and subsequently 873 K annealing, Mater. Des. 104 (2016) 355–364.
[40] Y. Matsukawa, H.L. Yang, K. Saito, Y. Murakami, T. Maruyama, T. Iwai, K. Murakami, Y. Shinohara, T. Kido, T. Toyama, The effect of crystallographic mismatch on the obstacle strength of second phase precipitate particles in dispersion strengthening: bcc Nb particles and nanometric Nb clusters embedded in hcp Zr, Acta Mater. 102 (2016) 323–332.
[41] N. Vermaak, G. Parry, R. Estevez, Y. Bréchet, New insight into crack formation during corrosion of zirconium-based metal-oxide systems, Acta Mater. 61 (2013) 4374–4383.
[42] A. Yilmazbayhan, A.T. Motta, R.J. Comstock, G.P. Sabol, B. Lai, Z. Cai, Structure of zirconium alloy oxides formed in pure water studied with synchrotron radiation and optical microscopy: relation to corrosion rate, J. Nucl. Mater. 324 (2004) 6–22.
[43] H. Kim, I. Kim, B. Choi, J. Park, Y. Jeong, K. Kim, Study of the corrosion and microstructure with annealing conditions of a β-quenched HANA-4 alloy, Corros. Sci. 52 (2010) 3162–3167.
[44] M. Kilo, R.A. Jackson, G. Borchardt, Computer modelling of ion migration in zirconia, Philos. Mag. 83 (2003) 3309–3325.
[45] L.J. Chai, B.F. Luan, S.S. Gao, J.W. Chen, Q. Liu, Study of precipitate evolution and recrystallization of β-quenched Zr–Sn–Nb–Fe–Cr–Cu alloy during aging, J. Nucl. Mater. 427 (2012) 274–281.
[46] H. Okamoto, Nb-Zr (niobium-zirconium), J. Phase Equilib. 13 (1992) 577.
[47] A.V. Nikulina, V.A. Markelov, M.M. Peregud, Y.K. Bibilashvili, V.A. Kotrekhov, A.F. Lositsky, N.V. Kuzmenko, Y.P. Shevnin, V.K. Shamardin, G.P. Kobylyansky, Zirconium alloy E635 as a material for fuel rod cladding and other components of VVER and RBMK cores, zirconium in the nuclear industry ASTM STP 1295, 9th International Symposium (1996) pp. 785–804.
[48] P. Bossis, D. Pecheur, L. Hanifi, J. Thomazet, M. Blat, Comparison of the high burn-up corrosion on M5 and low tin Zircaloy-4, J. ASTM Int. 3 (2006) 494–525.

[49] G. Sundell, M. Thuvander, H.O. Andrén, Barrier oxide chemistry and hydrogen pick-up mechanisms in zirconium alloys, Corros. Sci. 102 (2016) 490–502.
[50] W. Liu, B. Zhou, Q. Li, M. Yao, Detrimental role of LiOH on the oxide film formed on Zircaloy-4, Corros. Sci. 47 (2005) 1855–1860.
[51] S.S. Yardley, K.L. Moore, N. Ni, J.F. Wei, S. Lyon, M. Preuss, S. Lozano-Perez, C.R.M. Grovenor, An investigation of the oxidation behaviour of zirconium alloys using isotopic tracers and high resolution SIMS, J. Nucl. Mater. 443 (2013) 436–443.
[52] P. Tejland, H.O. Andrén, Oxidation induced localized creep deformation in Zircaloy-2, J. Nucl. Mater. 444 (2014) 30–34.
[53] L. Saintoyant, L. Legras, Y. Bréchet, Effect of an applied stress on the re-crystallization mechanisms of a zirconium alloy, Scr. Mater. 64 (2011) 418–421.
[54] P. Tejland, H.O. Andrén, Origin and effect of lateral cracks in oxide scales formed on zirconium alloys, J. Nucl. Mater. 430 (2012) 64–71.
[55] M. Guerain, C. Duriez, J.L. Grosseau-Poussard, M. Mermoux, Review of stress fields in zirconium alloys corrosion scales, Corros. Sci. 95 (2015) 11–21.
[56] N. Ni, D. Hudson, J. Wei, P. Wang, S. Lozano-Perez, G.D.W. Smith, J.M. Sykes, S.S. Yardley, K.L. Moore, S. Lyon, R. Cottis, M. Preuss, C.R.M. Grovenor, How the crystallography and nanoscale chemistry of the metal/oxide interface develops during the aqueous oxidation of zirconium cladding alloys, Acta Mater. 60 (2012) 7132–7149.
[57] I. Idarraga, M. Mermoux, C. Duriez, A. Crisci, J.P. Mardon, Potentialities of Raman imaging for the analysis of oxide scales formed on zircaloy-4 and M5® in air at high temperature, Oxid. Met. 79 (2013) 289–302.
[58] W. Qin, C. Nam, H.L. Li, J.A. Szpunar, Tetragonal phase stability in ZrO_2 film formed on zirconium alloys and its effects on corrosion resistance, Acta Mater. 55 (2007) 1695–1701.
[59] A. Garner, A. Gholinia, P. Frankel, M. Gass, I. MacLaren, M. Preuss, The microstructure and microtexture of zirconium oxide films studied by transmission electron backscatter diffraction and automated crystal orientation mapping with transmission electron microscopy, Acta Mater. 80 (2014) 159–171.
[60] M. Parise, O. Sicardy, G. Cailletaud, Modelling of the mechanical behavior of the metal–oxide system during Zr alloy oxidation, J. Nucl. Mater. 256 (1998) 35–46.